Observation of Organometallic and Radical Intermediates Formed during the Reaction of Methyl-Coenzyme M Reductase with Bromoethanesulfonate[†]

Xianghui Li,[‡] Joshua Telser,[§,||] Ryan C. Kunz,[‡] Brian M. Hoffman,[||] Gary Gerfen,[⊥] and Stephen W. Ragsdale*[,‡]

[‡]*Department of Biological Chemistry, University of Michigan, Ann Arbor, Michigan 48109,* [§]*Department of Biological, Chemical, and Physical Sciences, Roosevelt University, Chicago, Illinois 60605,* [||]*Department of Chemistry, Northwestern University, Evanston, Illinois 60208, and* [⊥]*Department of Physiology and Biophysics, Albert Einstein College of Medicine of Yeshiva University, Bronx, New York 10461*

ABSTRACT: Methyl-coenzyme M reductase (MCR) from methanogenic archaea catalyzes the final step of methane formation, in which methyl-coenzyme M (2-methylthioethanesulfonate, methyl-SCoM) is reduced with coenzyme B (*N*-(7-mercaptoheptanoyl)threonine phosphate, CoBSH) to form methane and the hetero-disulfide CoBS-SCoM. The active dimeric form of MCR contains two Ni(I)-F$_{430}$ prosthetic groups, one in each monomer. This report describes studies of the reaction of the active Ni(I) state of MCR (MCR$_{red1}$) with BES (2-bromoethanesulfonate) and CoBSH or its analogue, CoB$_6$SH (*N*-(6-mercaptohexanoyl)threonine phosphate), by transient kinetic measurements using EPR and UV−visible spectroscopy and by global fits of the data. This reaction is shown to lead to the formation of three intermediates, the first of which is assigned as an alkyl-Ni(III) species that forms as the active Ni(I)-MCR$_{red1}$ state of the enzyme decays. Subsequently, a radical (MCR$_{BES}$ radical) is formed that was characterized by multifrequency electron paramagnetic resonance (EPR) studies at X- (∼9 GHz), Q- (∼35 GHz), and D- (∼130 GHz) bands and by electron−nuclear double resonance (ENDOR) spectroscopy. The MCR$_{BES}$ radical is characterized by *g*-values at 2.00340 and 1.99832 and includes a strongly coupled nonexchangeable proton with a hyperfine coupling constant of 50 MHz. Based on transient kinetic measurements, the formation and decay of the radical coincide with a species that exhibits absorption peaks at 426 and 575 nm. Isotopic substitution, multifrequency EPR, and ENDOR spectroscopic experiments rule out the possibility that MCR$_{BES}$ is a tyrosyl radical and indicate that if a tyrosyl radical is formed during the reaction, it does not accumulate to detectable levels. The results provide support for a hybrid mechanism of methanogenesis by MCR that includes both alkyl-Ni and radical intermediates.

Methyl-coenzyme M reductase (MCR)[1] from methanogenic archaea catalyzes the final step of methane formation, in which methyl-coenzyme M (methyl-SCoM, 2-methylthioethanesulfonate) is reduced with coenzyme B (CoBSH, *N*-(7-mercaptoheptanoyl)threonine phosphate) to form methane and the hetero-disulfide CoBS-SCoM according to eq 1 (*1, 2*). The structures of these substrates and analogues described in this paper are shown in Scheme 1.

$$\text{methyl-SCoM} + \text{CoBSH} \rightarrow \text{CH}_4 + \text{CoBS-SCoM} \qquad (1)$$
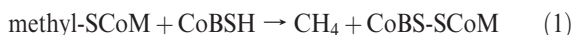
X-ray crystallographic studies have revealed that MCR is composed of three different subunits in an $(\alpha\beta\gamma)_2$ structure with an F$_{430}$ molecule in each of the two active sites (*3*). Coenzyme F$_{430}$, a redox-active nickel tetrahydrocorphin cofactor, noncovalently binds to MCR at the bottom of a 30 Å long hydrophobic well that accommodates the two substrates and shields the reaction from solvent. The phosphate group of CoBSH is

positioned by ionic interactions with MCR residues located halfway down this channel with its thiol group located 8.7 Å from the nickel. Methyl-SCoM binds in the pocket close to F$_{430}$ such that the thioether sulfur is positioned above the nickel and about 6.4 Å from the sulfur of CoBSH. There exist various oxidation and ligation states of F$_{430}$ in MCR, including EPR-active forms (MCR$_{red1}$, MCR$_{red2}$, MCR$_{ox1}$, and MCR$_{ox2}$) (*4*) and EPR-silent Ni(II) forms (MCR$_{silent}$, MCR$_{red1-silent}$, and MCR$_{ox1-silent}$) (*3, 5, 6*). MCR$_{red1}$ with Ni(I)-F$_{430}$ is known to be the active form of MCR and exhibits characteristic EPR spectra with the following *g*-values: $g_\perp = 2.065$, $g_\parallel = 2.24$ (*7−9*).

The active MCR$_{red1}$ state has been shown to undergo a variety of reactions, some of which lead to EPR-detectable species. In the presence of HSCoM and CoBSH, the MCR$_{red1}$ state is partly converted into the MCR$_{red2}$ state, which has a rhombic Ni(I)-type EPR signal (*10*). The reaction of MCR$_{red1}$ with various alkyl bromides leads to the formation of organometallic alkyl-Ni species. For example, the reaction of MCR$_{red1}$ with 3-bromo-propanesulfonate (BPS), the most potent known inhibitor of methanogenesis (*11*), generates MCR$_{PS}$ (originally termed MCR$_{BPS}$ (*12*)), which is an organometallic Ni(III)/propyl sulfonate species in resonance with a Ni(II)/propyl sulfonyl radical (*13*). The EPR spectrum of MCR$_{PS}$ exhibits *g*-values at 2.108, 2.112, and 2.219, with most (∼75%) of the spin density located in the nickel 3d($x^2 − y^2$) orbital (*13*). Similarly, when MCR$_{red1}$ is

[1]Abbreviations: MCR, methyl-coenzyme M reductase; BES, bromoethanesulfonate; BPS, 3-bromopropanesulfonate; DFT, density functional theory; ENDOR, electron−nuclear double resonance; EPR, electron paramagnetic resonance; HF, high frequency; HSCoM, coenzyme M; CoBSH, coenzyme B; rf, radiofrequency.

Scheme 1: Structures of HSCoM Analogues
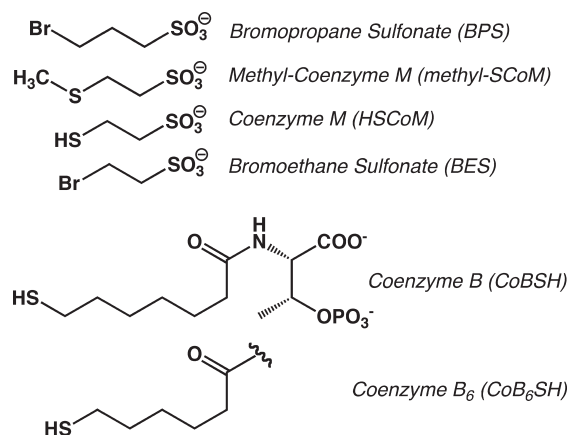
reacted with methyl iodide or methyl bromide, an organometallic methyl-Ni(III) species is formed (MCR$_{Me}$) (*14, 15*). Similar organo-Ni(III) species are generated when MCR$_{red1}$ is reacted with various brominated acids (*16*). Both MCR$_{Me}$ and MCR$_{PS}$ can be converted to the active MCR$_{red1}$ state under certain conditions, for example, by reaction with thiolates like HSCoM (*12, 16, 17*).

While MCR$_{red1}$ reacts with BPS to generate an organo-Ni(III) species, the reaction of MCR$_{red1}$ with 2-bromoethanesulfonate (BES) in the presence of CoBSH generates a radical (MCR$_{BES}$ radical), characterized by a doublet EPR signal (*18*). BES is a reversible inhibitor that is competitive with respect to methyl-SCoM (*19, 20*) and has also been used to inhibit methanogenesis within the bovine rumen (*21*). Several other methyl-SCoM analogues, (3-bromopropionate, cyano-coenzyme M, seleno-coenzyme M, and trifluoromethyl-coenzyme M), also have been shown to induce the doublet radical EPR signal when they are reacted with MCR$_{red1}$ in the presence of CoBSH (*18*). The studies described in the current report were focused on obtaining a better understanding of the nature of the reaction of MCR with BES. Prior studies indicated that reactive haloalkyl compounds that are the size of HSCoM generate radicals and those that are the size of methyl-SCoM (and larger) generate organometallic species, suggesting that subtle changes in length of the reactive inhibitor (e.g., BPS versus BES) reflect the extreme selectivity in the MCR active site. However, as shown here, the reaction with BES also generates an organometallic intermediate that rapidly converts to the characteristic MCR$_{BES}$ radical. Therefore, when comparing various haloalkanes, the nature of the intermediates actually may not change; instead, the rates of formation and decay of the organometallic, radical, and other intermediates vary, thus altering the amount of these species that can accumulate.

Three types of mechanisms for MCR-based catalysis have been proposed, mechanism I involving an organometallic methyl-Ni intermediate (*6, 22*), mechanism II involving a methyl radical (*23*), and mechanism III, which involves methyl-Ni and interactions between the substrate and the tetrapyrrole ring of F$_{430}$ (*24*). Mechanism I, proposed based on the crystal structure (*3*) and mechanistic work with F$_{430}$ model complexes (*25–27*), involves nucleophilic attack of Ni(I)-MCR$_{red1}$ on the methyl group of methyl-SCoM to generate a methyl-Ni intermediate (*17*). Mechanism III starts with protonation of coenzyme F$_{430}$ (*42*), which promotes reductive cleavage of the methyl-SCoM thioether bond generating a nickel center that is coordinated by $^-$CH$_3$ and $^-$SCoM anions and two of the tetrapyrrole nitrogens. The CoBS$^-$ anion is then proposed to react with $^-$SCoM to form the

heterodisulfide product and methyl-Ni(I). Formation of methane requires the proton that was initially donated to coenzyme F$_{430}$. Mechanism I is supported by the characterization of various alkyl-Ni species that have been generated by the reaction of MCR$_{red1}$ with 3-bromopropionate (BPS) and other alkyl halides (*14, 16, 28*). In addition, MCR$_{PS}$ and other alkyl-Ni(III) species can be converted to the active MCR$_{red1}$ state by reacting with organic thiolates, which forms a thioether product (*17*). Mechanism II is based on density functional theory (DFT) computations and proposes that Ni(I) attacks the sulfur atom of methyl-SCoM, promoting homolytic cleavage of the methyl–sulfur bond and generating a MCR$_{ox1}$-like Ni(III)-SCoM complex and a methyl radical, which abstracts a hydrogen atom from CoBSH to generate methane (*23, 29, 30*).

Mechanisms I–III remain viable because neither the methyl-Ni(III) intermediate nor the Ni(III)-SCoM species has been observed upon reaction of MCR$_{red1}$ with the native substrate methyl-SCoM. In fact, no spectroscopic changes have been reported when MCR$_{red1}$ is reacted with the native substrates either separately or together, regardless of the order of addition or the concentration of the substrates. Thus, in order to probe the reaction mechanism, substrate analogues have been used. Among these, 2-bromoethanesulfonate (BES) is similar in size to methyl-SCoM and contains an excellent leaving group (Br$^-$), promoting a rapid reaction with MCR.

Here, rapid kinetic and spectroscopic experiments were performed to better understand the reaction of MCR$_{red1}$ with BES in the presence of CoBSH or an analogue, *N*-(6-mercaptohexa-noyl)threonine phosphate (CoB$_6$SH). The combined results indicate that formation of the MCR$_{BES}$ radical is a three-step reaction and that the first step involves formation of a transient alkyl-Ni(III) species that rapidly decays to form the doublet radical species. The UV–visible spectra indicate that the radical has long wavelength absorption (∼575 nm). Isotopic substitution coupled with EPR and ENDOR experiments also rule out the possibility that the radical originates from one of the two Tyr residues located directly above the active site Ni center.

MATERIALS AND METHODS

Materials. Methanothermobacter marburgensis was obtained from the Oregon Collection of Methanogens (Portland, OR) catalog as OCM82. CoBSH and CoB$_6$SH were synthesized from 7-bromoheptanoic acid and 6-bromohexanoic acid, respectively, as described previously (*28, 31, 32*). The purities of CoBSH and CoB$_6$SH were ascertained to be >98% by ^{1}H NMR. [^{2}H$_6$]-*p*-hydroxyphenylacetic acid was prepared from *p*-hydroxyphe-nylacetic acid as described (*33*). The yield was measured by mass spectrometry with the following distribution of deuterium: 80% of [^{2}H$_6$]-, 18% of [^{2}H$_5$]-, and 2% of [^{2}H$_4$]-*p*-hydroxyphenylace-tic acid. Other reagents were purchased from Sigma-Aldrich. N$_2$ (99.98%), H$_2$/CO$_2$ (80%/20%), and ultrahigh purity H$_2$ (99.999%) were obtained from Cryogenic Gases (Detroit, MI).

Protein Purification. The purification of MCR$_{red1}$ from *M. marburgensis* was performed under strictly anaerobic condi-tions, as described previously (*17*). According to the UV–visible spectrum (representative spectra are shown below), 50–70% of MCR$_{red1}$ was typically generated. MCR$_{red1}$, which was uni-versally labeled with [^{2}H$_6$]Tyr, was generated by culturing *M. marburgensis* in the presence of 3 mM [^{2}H$_6$]-*p*-hydroxyphe-nylacetic acid, 0.1 mM phenylacetate, and 0.02 mM indoleace-tate, which are precursors of Tyr (*M. marburgensis* does not appear to import Tyr) (*33*). Peptide hydrolysis followed by mass

spectrometric and amino acid analyses was used to determine the amount of [^{2}H$_6$]-*p*-hydroxyphenylacetic acid incorporated into the tyrosine residues in MCR. For amino acid analysis, MCR was hydrolyzed using 6 M HCl for 24 h at 110 °C, and then the amino residues were treated with bis(trimethylsilyl)trifluoroacetamide (BSTFA) and acetonitrile (1:1 v/v) for 1 h at 100 °C. These trimethylsilyl derivatives were analyzed using a Finnigan Trace GC/MS. O-Acetylation of tyrosine in MCR was obtained through treatment of 130 μM MCR with 280 mM *N*-acetylimidazole on ice for 2.5 h. The excess *N*-acetylimidazole was removed with a molecular weight cutoff centrifugal filter.

Spectroscopy of MCR. UV−visible spectra of MCR were recorded in the anaerobic chamber using a diode array spectrophotometer (model DT 1000A; Analytical Instrument Systems, Inc., Flemington, NJ). X-band EPR spectra were recorded on a Bruker EMX spectrometer (Bruker Biospin Corp., Billerica, MA), equipped with an Oxford ITC4 temperature controller, a Hewlett-Packard model 5340 automatic frequency counter, and Bruker gaussmeter. Spin concentration was determined by double integration of the sample spectrum obtained under nonsaturating conditions and comparing to that of 1 mM copper perchlorate standard. All samples for EPR spectroscopy were prepared in 50 mM Tris buffer, pH 7.6, in a Vacuum Atmospheres anaerobic chamber (Hawthorne, CA) maintained under nitrogen gas at < 1 ppm of oxygen.

CW 35 GHz ("Q-band") EPR and ENDOR (*34*) spectra were recorded on a modified Varian E-110 spectrometer equipped with a helium immersion dewar at 2 K under "rapid passage" (*35*) conditions using 100 kHz field modulation (*36*). Under these conditions, the EPR spectrum appears as an absorption line shape, rather than in first derivative mode. Pulsed 35 GHz echodetected EPR and ENDOR spectra were obtained at 2 K on a locally constructed spectrometer (*37*). For the echo-detected EPR spectra, the signal intensity of a standard Hahn two-pulse spin echo is monitored as a function of field sweep. Multiple echo intensities are averaged, and the EPR spectrum can be recorded at various repetition rates to probe the relaxation behavior of multiple paramagnetic sites within a sample. The line shape of such an echo-detected EPR spectrum may show distortions from that expected for an ideal powder pattern as the phase of the spin echo can vary during the data acquisition, due to instrumental limitations. More importantly, the T_1 is not a constant over the EPR envelope, even for a single paramagnetic site. As it is also not experimentally feasible to wait enough multiples of the longest T_1 between pulse cycles to allow full recovery of the magnetization (ideally, a repetition rate $> 10T_1$), the degree of saturation and hence the intensity vary across the spectrum, distorting it. Echo-detected EPR spectra necessarily appear as the absorption line shape, so that the 35 GHz CW and pulsed EPR spectra have the same general appearance.

For the CW ENDOR spectra (*34*), two methods were employed: sweeping the rf (in either direction), as is commonly done (*36*), or by random hopping of the rf using a sample time, delay time, and rf time, as has been recently developed (*38*). This latter stochastic method avoids many of the line shape artifacts found in swept CW ENDOR spectra (*39*) but generally gives a lower signal/noise ratio. For the pulsed 35 GHz ENDOR spectra, the Mims three-pulse ENDOR sequence, $t_{mw}-\tau-t_{mw}-T(rf)-t_{mw}-\tau-$echo (*34, 40*), was employed, where t_{mw} is the $\pi/2$ microwave pulse length (typically 50 ns), τ is a preparation (or delay) time (typically 500 ns), and $T(rf)$ is the time during which the rf is applied (typically 60 μs). The Mims sequence has the property

that its ENDOR intensities follow the relationship $I(A) \sim 1 - \cos(2\pi A\tau)$, where A is the hyperfine coupling of a given nucleus. As a result, the signals vanish (give "blind spots") at $A\tau = n, n = 0, 1, ...,$ and show maximum intensities at $A\tau = n + \frac{1}{2}$. However, the chief use of pulsed ENDOR in this work was to observe very weakly coupled ^{2}H signals, so that this suppression effect is of little consequence. Pulsed ENDOR measurements were implemented with random hopping of the radio frequency over the frequency range for a spectrum, a procedure that improves intensity and signal shape.

The ENDOR pattern for a single orientation of an $I = \frac{1}{2}$ nucleus with relatively small hyperfine coupling and large g_N, as is the case for ^{1}H, exhibits a $\nu(\pm)$ doublet that is centered at the nuclear Larmor frequency, ν_N, and split by half the hyperfine coupling, $|A/2|$. For an $I = 1$ nucleus, such as ^{2}H, there is quadrupole splitting such that each hyperfine-split doublet is further split into $2I$ lines. However, if the hyperfine and quadrupole couplings are of similar magnitude, then this first-order pattern is not obtained. For typical conditions used here, $g \sim 2.0$, $\nu_{mw} \sim 35$ GHz, and $B_0 = 1.25$ T, so that $\nu(^1H) \approx 53$ MHz and $\nu(^2H)) \approx 8.2$ MHz.

High-frequency (130 GHz, "D-band") EPR and ENDOR spectra were obtained on a spectrometer described previously (*41, 42*). Field swept two-pulse (Hahn) echo-detected spectra were registered with 0/180° phase cycling of the first microwave pulse to eliminate baseline artifacts. Specific acquisition parameters are given in the figure legend.

Kinetic Assay. To follow the slow kinetics related to radical decay, a diode array spectrophotometer (model DT 1000A; Analytical Instrument Systems, Inc., Flemington, NJ) was used. For observation of the rapid reaction related to radical formation, stopped-flow experiments were carried out on an Applied Photophysics spectrophotometer (SX.MV18; Leatherhead, U.K.) equipped with a photodiode array detector. The stopped-flow instrument was located in a Vacuum Atmospheres anaerobic chamber. In these mixing experiments, one syringe contained a solution consisting of 30 μM MCR$_{red1}$ and CoBSH (or CoB$_6$SH), and the other contained BES. The concentrations of CoBSH (or CoB$_6$SH) and BES were varied in independent experiments. All experiments were performed in 50 mM Tris-HCl buffer, pH 7.6, at room temperature in the anaerobic chamber maintained at < 0.5 ppm O$_2$. Data were globally fit using the software prokineticist v1.06 (Applied Photophysics Ltd., Leatherhead, U.K.).

RESULTS

Optical Spectroscopy. Upon addition of BES to MCR$_{red1}$ in the presence of CoB$_6$SH, the absorption maximum of MCR$_{red1}$ (Figure 1, solid line) at 385 nm shifts to 426 nm. Furthermore, the Ni(I)-associated peak at 720 nm disappears while a broad peak around 575 nm appears (dashed line), as clearly shown by the difference spectrum given in the inset. As described below, these absorption changes coincide with the formation of an EPR-active species that we will call "MCR$_{BES}$", or the "MCR$_{BES}$ radical". The maximum difference absorption peaks associated with formation of the MCR$_{BES}$ radical include a rather sharp peak at 442 nm and a broader band around 575 nm. The addition of CoB$_6$SH alone has no effect on the UV−visible spectrum of MCR$_{red1}$, while the addition of BES alone results in decay of the 385 and 720 nm bands of MCR$_{red1}$ without the appearance of the absorption feature at 575 nm.

The radical species generated by the reaction of MCR$_{red1}$ in the presence of CoB$_6$SH with BES is relatively stable; after 1 h, the
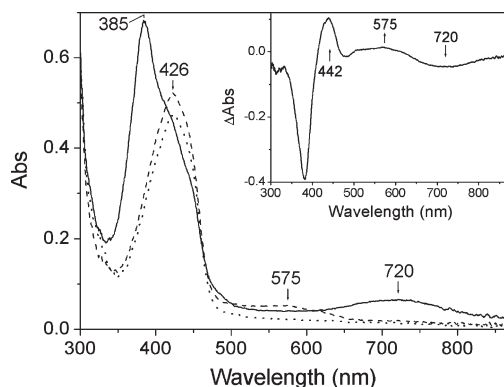
FIGURE 1: Visible spectra of the MCR$_{BES}$ radical before (solid line), 30 s (dashed line) and 1 h (dotted line) after addition of 2 mM BES to a solution of 21 μM MCR$_{red1}$ and 0.5 mM CoB$_6$SH. Inset: difference spectrum of dashed line minus solid line.
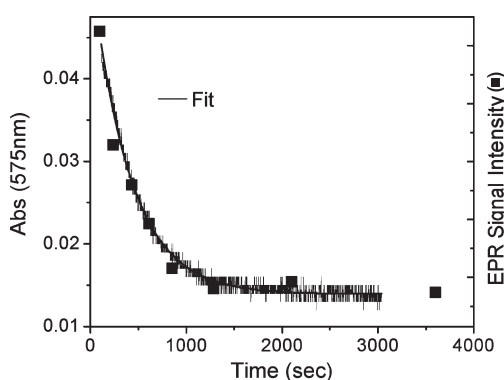

FIGURE 2: Slow kinetics of MCR$_{BES}$ radical decay after reaction of MCR$_{red1}$ with BES in the presence of CoB$_6$SH followed by visible (left) and EPR spectroscopy (squares).

peak at 426 nm slightly decreases as the 575 nm peak disappears (Figure 1, dotted line). The rates at which the absorption bands at 426 and 575 nm decrease were measured by fitting the data to a single-exponential decay function (Figure 2), revealing a decay rate constant of 0.0021 ± 0.0003 s^{-1}. When the solution containing MCR$_{red1}$ and the native substrate CoBSH was reacted with BES, the decay rate constant was ~10-fold slower (0.00020 ± 0.00008 s^{-1}; see Figure S1, Supporting Information). Thus, the presence of the native substrate CoBSH stabilizes the MCR$_{BES}$ radical (relative to CoB$_6$SH).

EPR Spectroscopy. Addition of BES to a solution of MCR$_{red1}$, which is characterized by g-values at $g_\perp = 2.065$, $g_\parallel = 2.24$ (Figure 3A), containing CoB$_6$SH led to decay of the MCR$_{red1}$ X-band EPR signal (measured at 70 K) coupled to the generation of a radical signal centered at $g \approx 2.002$ with a doublet splitting of approximately 17 G (Figure 3B); a simulation of this signal using an isotropic ^{1}H hyperfine coupling of 50 MHz is also included. The peaks with values of $g_\perp = 2.16$ and $g_\parallel = 2.23$ derive from the MCR$_{ox1}$ state, which exists in variable proportions in MCR samples and has been assigned to a Ni(III)-thiolate species in resonance with a Ni(II)-thiyl radical (*43, 44*). There are small features at a g-value of 2.07, which is characteristic of MCR$_{red2}$ (*45*), and at $g \sim$2.14 (of unknown origin) that are more easily resolved in the 35 GHz EPR spectrum (Figure S1, Supporting Information) but are not related to the scope of this investigation on the MCR$_{BES}$ radical. As shown in Figure 3, the EPR signal from MCR$_{ox1}$ is not affected by the reaction with CoB$_6$SH and BES, indicating that only the Ni(I) state of MCR
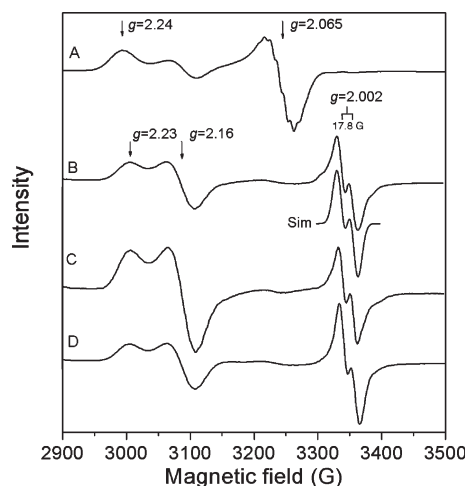

FIGURE 3: EPR spectra of 150 μM MCR$_{red1}$ (A) after addition of 1.5 mM CoB$_6$SH and 1.5 mM BES in H$_2$O (B) and D$_2$O (C). The EPR spectrum in (D) was obtained after reacting MCR$_{red1}$ containing universally labeled [^{2}H$_6$]Tyr residues under identical conditions as in (B).

reacts with BES in the presence of CoB$_6$SH. This MCR$_{BES}$ radical signal is also observed when MCR$_{red1}$ is reacted with BES in the presence of the native substrate, CoBSH (data not shown). As with the UV–visible experiments, both BES and CoBSH (or CoB$_6$SH) are required for radical formation; no changes in the MCR$_{red1}$ EPR spectrum are observed when CoB$_6$SH or CoBSH alone is added, and when only BES is added, the Ni(I) state of MCR oxidizes to EPR-silent Ni(II).

To test the hypothesis that formation of the MCR$_{BES}$ EPR signal is coupled to the UV–visible spectra with difference peaks at 442 and 575 nm, freeze–quench EPR experiments were performed under conditions similar to the stopped-flow experiments described above (Figure 2). Thus, when a solution of MCR$_{red1}$ and CoB$_6$SH was reacted with BES, the EPR signal of the MCR$_{BES}$ radical decayed with the same rate constant (0.0021 ± 0.0003 s^{-1}) (Figure 2, squares) that was measured by UV–visible spectroscopy (above, 0.0021 s^{-1}). These experiments indicate that the 575 nm peak observed in the UV–visible spectrum and the MCR$_{BES}$ radical EPR spectrum originate from the same species.

To determine if the MCR$_{BES}$ radical contains exchangeable protons, the reaction of MCR$_{red1}$ with CoB$_6$SH and BES was carried out in both H$_2$O and D$_2$O, and the resultant solutions were examined by EPR and ENDOR spectroscopic experiments. As shown in Figure 3C, the ^{1}H doublet splitting in the X-band EPR spectrum of the radical is unchanged when the reaction is performed in D$_2$O, demonstrating that the hyperfine splitting of the MCR$_{BES}$ radical is not associated with a solvent-exchangeable hydrogen nucleus.

Accurate assignment of the g-values in the EPR spectra of organic radicals can aid in the identification of the radical. To obtain highly accurate g-values for the MCR$_{BES}$ radical, we recorded high-frequency (HF) EPR spectra at 130 GHz (D-band). This high microwave frequency has the advantage of yielding better resolution of multiple EPR-active species in a heterogeneous sample (i.e., by providing greater dispersion of g-values) and of revealing features that permit determination of the full **g** tensor of seemingly isotropic radical centers. Although the MCR$_{BES}$ radical appeared as a doublet with an isotropic $g = 2.00$, in the X-band EPR spectra, the Hahn echo-detected 130 GHz EPR spectrum displays approximate axial symmetry and lies entirely below $g = 2.005$ (Figure 4). Although the majority of
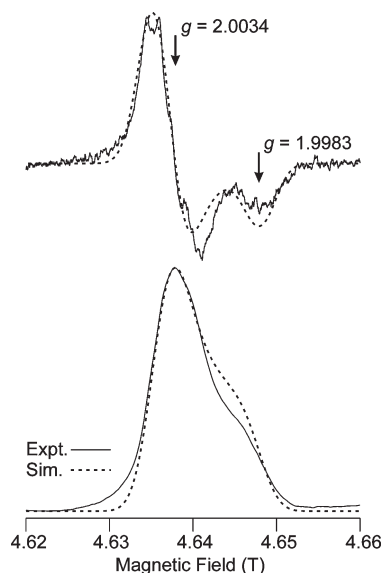
FIGURE 4: High-frequency (130 GHz) two-pulse (Hahn) echo-detected EPR spectrum of MCR_{red1} reacted with CoB_6SH and BES for 1 min and then frozen.

FIGURE 5: Broad scan "stochastic" CW 35 GHz ^1H ENDOR spectra recorded at 2 K of MCR_{red1} in the presence of 1 mM CoB_6SH after addition of BES at a field position on the radical signal (blue trace; $g = 2.008$) and at one on the MCR signal (red trace; $g = 2.175$).

the spectrum appears to originate from a single radical species, it is possible that a small amount ($<10\%$) of a minority species is present. Structure is evident in Figure 4, but its origin is not known at this point, and no attempt was made to simulate it.

Simulation of the D-band EPR spectrum yielded $g_\perp = 2.0034$ and $g_\parallel = 1.9983$. This ability to accurately determine the **g** tensor of the MCR_{BES} EPR signal in the HF spectra comes at the cost of increased line width due to g-strain (*46*). In the present case, the single-crystal line width increases from 27 MHz at X-band to 60 MHz at D-band, so that the 17 G splitting evident in the X-band spectra (Figure 1A) is no longer resolved (simulations of the D-band spectrum were almost identical whether or not an isotropic ^1H hyperfine splitting of 50 MHz, as determined at X-band, was included). Likewise, the resolved ^{14}N hyperfine splitting at $g_\perp$ of the MCR_{red1} signal (from the F_{430} pyrrole/pyrroline ligands (*43, 45*)) evident in the X-band spectrum is not resolved in the 130 GHz or the 35 GHz spectra (see Figure S2, Supporting Information).

Q-Band (35 GHz) and D-Band (130 GHz) ENDOR Spectroscopic Experiments. The 35 GHz ENDOR methodology employed here uses a temperature of 2 K, which is best suited to metal-centered paramagnets. Thus, it was comparatively easy to record good quality spectra on field positions of the MCR Ni signals (e.g., $g \sim 2.17$), which readily showed the ν_+ partner of the strongly coupled ($A(^1H) = 28$ MHz) signal that has been attributed to a hydrido ligand (denoted H_{rh}) to Ni(III) in MCR_{red2a} (*47*). This signal can be seen in Figure 5. In this case, CW ENDOR with random hopping of the rf was employed, which gives a better baseline. A corresponding swept ENDOR spectrum is shown in Figure S3 (Supporting Information). In contrast, spectra recorded at the field position of the radical signal ($g \sim 2.00$) were of lower signal/noise ratio and did not exhibit any strongly coupled protons; only those with $A(^1H) < \sim12$ MHz were observed, as also seen in Figure 5. Swept rf CW ^1H Q-band ENDOR spectra recorded at $g \sim 2.00$ (radical signal) and at $g \sim 2.17$ (MCR signal) are shown in Figure S3 (Supporting Information). Under these conditions, the ^1H ENDOR signal has a higher signal/noise ratio. There appear to be signals extending to >20 MHz from $\nu(^1H)$, so that the maximum hyperfine

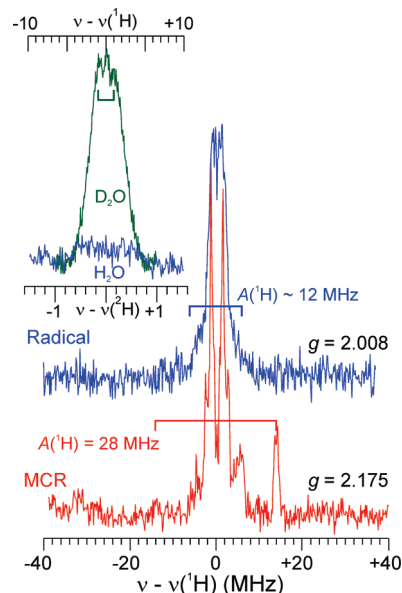coupling may be >40 MHz, in agreement with the X-band EPR results. Note that at 35 GHz the radical EPR signal still appears isotropic (in contrast to the 130 GHz result, Figure 4). As a result, there is no "orientation selection" (*34*) in the ENDOR, in contrast to the anisotropic MCR signal(s), which leads to broader ENDOR lines and greater difficulty in determining the $A(^1H)$ tensor. No significant differences were seen in the ^1H pattern for H_2O versus D_2O samples.

The use of ^2H ENDOR facilitates focusing on the question of solvent exchange more directly. Figure 5 (inset) compares the 35 GHz Mims ^2H ENDOR spectra of the MCR_{BES} samples generated in H_2O and D_2O, recorded at the field position corresponding to the maximum intensity of the radical signal. The sample in D_2O showed a largely unresolved matrix ^2H ENDOR signal centered at the ^2H Larmor frequency that is essentially the same when recorded at varying field positions on the EPR envelope of the radical signal. Superimposed on this is a poorly resolved splitting, which might be assigned to $A(^2H) \approx 0.3$ MHz (corresponding to $A(^1H) \approx 2$ MHz, which is well inside the overall ^1H CW ENDOR pattern, Figure S1 (Supporting Information)).[2] In summary, the combined ENDOR and EPR results rule out the possibility that the doublet splitting seen in the X-band EPR spectrum derives from an exchangeable proton.

Isotopic Substitution and EPR/ENDOR Spectroscopic Experiments To Determine If the MCR_{BES} Species Derives from a Tyrosyl Radical. Based on the crystal structure of MCR (*3*), there are a number of viable candidates for the relatively stable MCR_{BES} radical. These include αTyr333 (4.3 Å from Ni), βTyr367 (4.3 Å from Ni), αthioglycine445 (12 Å from Ni), the sulfur of CoBSH (8.87 Å away from Ni) (*6*), or the corphin ring itself. Given how close αTyr333 and βTyr367 are to the Ni active site, they seemed to be the most likely contenders.

Tyrosyl radicals are widely found in enzymes, including the photosynthetic oxygen evolving complex (OEC) (*48, 49*),

---

[2]Deuterium signals also were not observed in the D-band (130 GHz) ENDOR spectra of samples of MCR_{red1} that had been exchanged with D_2O and incubated with BES and CoB_6SH (not shown).

prostaglandin H synthase (PGHS) (*50, 51*), ribonucleotide reductase (RNR) (*52*), and galactose oxidase (*53, 54*). The low-frequency (X-band) EPR spectra of tyrosyl radicals are dominated by hyperfine coupling to nonexchangeable protons. Each of the two ring protons ortho to the phenol oxygen has an anisotropic coupling, the largest component of which is typically in the 20–30 MHz range. The two side-chain methylene protons have an approximately isotropic coupling, the values of which are highly dependent on the dihedral angle with respect to the ring plane normal. Depending on the angle, the coupling of these protons may range from ∼0 to >60 MHz. However, no matter what the angle, at least one methylene proton will experience a significant (>10 MHz) hyperfine coupling. The variability of the side chain dihedral angle, and resulting variability of the methylene proton hyperfine couplings, means that the X-band spectra of tyrosyl radicals can display a variety of splitting patterns. But all tyrosyl radical spectra experience significant spectral splittings and/or width from the hyperfine coupling of three or four nonexchangeable protons, and thus the substitution of natural abundance tyrosine by an isotopologue that is deuterated at *any* position would be expected to have an observable spectral impact for any tyrosyl radical species.

Unlike X-band spectra, the D-band spectra of tyrosyl radicals are dominated by the (field-dependent) Zeeman interaction, which is gauged by *g*-values. Unmodified tyrosyl radicals have an anisotropic (rhombic) *g*-matrix with principal values that are fairly consistent: g_x (or g_1) is in the range of 2.009–2.006 depending on the electrostatic/hydrogen bonding environment of the phenol oxygen, g_y (or g_2) ∼ 2.004–2.005, and g_z (or g_3) ∼ 2.002–2.003. Thus, by using HFEPR to determine the *g*-values, as well as X-band EPR and Q-band ENDOR to measure the hyperfine couplings of the radical in the enzyme prepared with both protonated and deuterated tyrosine, we sought to provide definitive evidence for or against the radical species originating from tyrosine, specifically αTyr333 or βTyr367.

Samples of MCR were generated that contained a tyrosine isotopologue. MCR_{red1} was globally labeled with [$^2H_6$]Tyr by feeding *M. marburgensis* cells with [$^2H_6$]hydroxyphenylacetate; then MCR was isolated and digested, and the amino acids were analyzed with GC-MS. The results showed that at least 50% of tyrosine residues in MCR were labeled with [$^2H_4$]Tyr instead of [$^2H_6$]Tyr. This is a lower estimate of the labeling percentage because significant H-exchange occurs during the acid hydrolysis. A similar estimate of the labeling percentage was obtained by mass spectrometric analysis of BrCN- and AspN-digested fragments of MCR isolated from cells grown on labeled hydroxyphenylacetate; e.g., greater than 50% of βTyr367 was labeled (Figure 6). Even though the fragment including αTyr333 was not identified, 11 other peptides containing tyrosine residues showed a similar percentage of [$^2H_6$]Tyr labeling. Thus, independent amino acid and peptide analyses confirmed that the Tyr residues in MCR were significantly labeled when cells were fed with [$^2H_6$]hydroxyphenylacetate under the conditions described.

In order to test the hypothesis that the radical intermediate detected by EPR and UV–visible spectroscopic studies derives from Tyr, [$^2H_6$]Tyr-labeled MCR_{red1} was reacted with BES in the presence of CoB_6SH. If the EPR spectra were associated with one of the two Tyr residues located immediately above the Ni center at the active site of MCR, then a significant change in the line shape would be expected upon substitution of these [$^1H_6$]Tyr residues with [$^2H_6$]Tyr. As shown in Figure 3D, the EPR spectrum of the MCR_{BES} radical appeared unchanged by the [^2H]Tyr
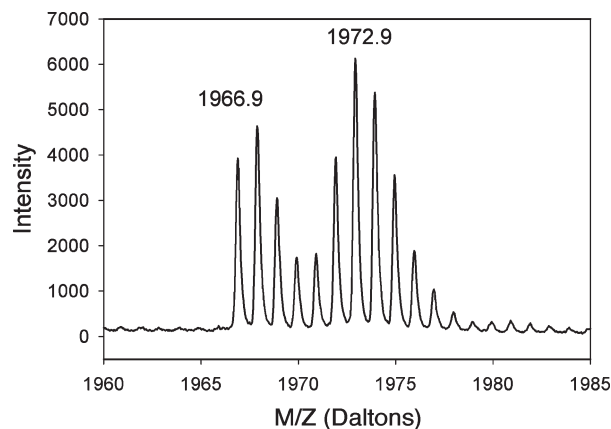

FIGURE 6: Mass spectrum of the fragment containing βTyr367 (IYGGGGPGIFNGNHIVTRH), which is located directly above the Ni center in F_{430}.
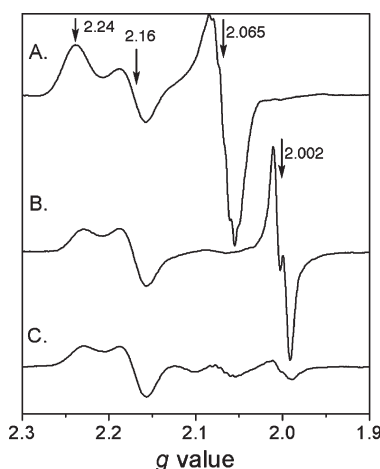

FIGURE 7: X-band EPR spectra of 100 μM MCR_{red1} after reaction with (A) acetylimidazole, (B) with 5 mM BES in the presence of 1 mM CoB_6SH, and (C) with 5 mM BES and 1 mM CoB_6SH (as in (B)) and acetylimidazole.

substitution, with the same degree of hyperfine splitting remaining in the MCR_{BES} radical. These experiments unambiguously rule out the possibility that MCR_{BES} contains a tyrosyl radical.

Pulsed 35 GHz ENDOR spectra of the sample containing [$^2H_6$]Tyr exhibited a very weak and featureless signal centered at the deuteron Larmor frequency. Essentially the same signal (not shown) was observed at multiple positions on the EPR envelope. This ^2H signal may arise from distant coupling to the various paramagnetic centers that make up the overall EPR envelope. The ^1H ENDOR spectrum of this sample was indistinguishable from the samples with natural abundance tyrosine whether in H_2O or D_2O solvent.

Effect of Tyrosyl Acetylation. Even though the EPR experiments clearly show that the MCR_{BES} radical is not a tyrosyl radical, the tyrosyl residues still appear to play an important role in radical formation. As shown in Figure 7A, acetylation of tyrosyl residues in MCR_{red1} by treatment with *N*-acetylimidazole has no effect on the EPR spectrum of MCR_{red1}; however, Tyr acetylation blocks the formation of the MCR_{BES} radical. As shown in Figure 7C, the amount of MCR_{BES} generated from the reaction of acetylated MCR_{red1} with BES and CoB_6SH was greatly decreased and some MCR_{red1} remains, as compared with the reaction of unlabeled MCR_{red1} with BES and CoB_6SH (Figure 7B).
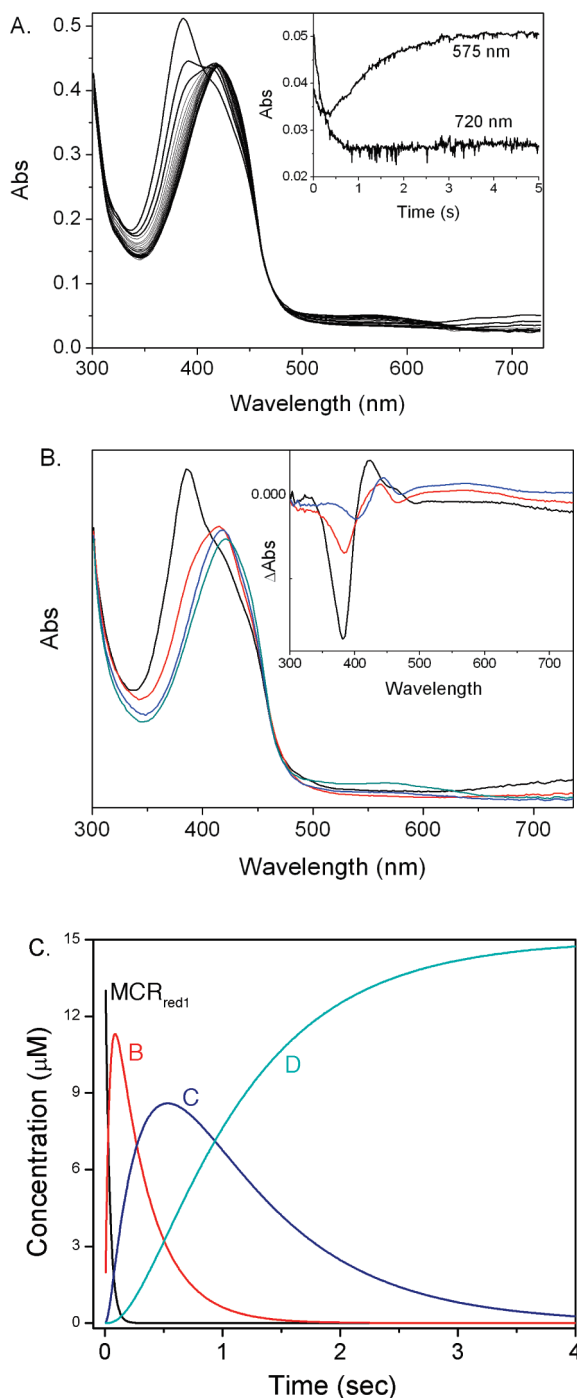
FIGURE 8: Time course and spectral intermediates in the reaction of MCR_red1 with BES and CoB6SH.

Kinetics of MCR_BES Radical Formation. The MCR_BES radical is formed rapidly, and the transient kinetics were followed by stopped-flow with UV−visible spectroscopy (Figure 8A). The kinetic data ranging from 350 to 732 nm were globally fit to a four-component equation (eq 2).

$$A \xrightarrow{k_1} B \xrightarrow{k_2} C \xrightarrow{k_3} D \qquad (2)$$

Two spectral intermediates, B (Figure 8B, red line) and C (Figure 8B, blue line), and D (associated with the MCR_BES radical) were identified. The difference spectra between A and B (Figure 8B inset, black line) showed that a new species with absorption at 420 nm and a shoulder at 457 nm was formed accompanying the decay of the 385 and 720 nm bands of
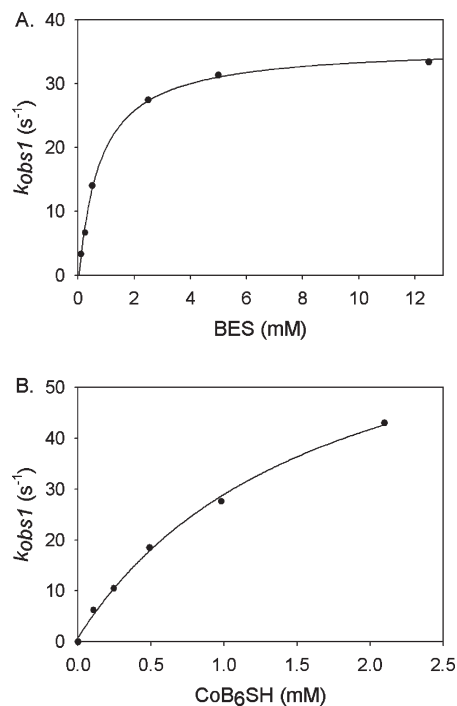

FIGURE 9: Concentration dependence of the rate of MCR_BES radical formation.

MCR_red1. It has been shown that the shoulder around 457 nm is characteristic of the methyl-Ni(III) species of MCR (*14*); thus, we assign intermediate B as an alkyl-Ni(III) species. The 457 nm peak then disappears as intermediate B converts to intermediate C, which appears to be a Ni(II) species. In the last step, the MCR_BES radical (species D) forms.

By varying the concentration of BES (Figure 9A) or CoB6SH (Figure 9B), the first step in this three-step sequence (with rate constant k_{obs1}) was shown to be dependent on the concentrations of both CoB6SH and BES, while k_{obs2} and k_{obs3} were independent of the CoB6SH or BES concentrations. The k_{obs1} was fit to eq 3 to derive the values of k_1 and K_m, where [S] is the concentration of CoB6SH or BES.

$$k_{obs1} = \frac{k_1[S]}{K_m + [S]} \qquad (3)$$

The rate constants for the three steps are provided in Table 1. The conversion of A to intermediate B gives a second-order rate constant of $45000 \text{ M}^{-1} \text{ s}^{-1}$, the conversion of intermediate B to C has a rate constant of 2.6 s^{-1}, and formation of the MCR_BES radical (species D) occurs with a rate constant of 1.0 s^{-1}. As shown above, decay of species D occurs with a rate constant of 0.0021 s^{-1} (not given in Table 1).

DISCUSSION

Transient kinetics combined with UV−visible and EPR spectroscopic experiments have revealed the accumulation of three intermediates during the reaction of the active Ni(I)-MCR_red1 with the substrate analogues CoB6SH and BES (Figure 8). Figure 10 describes the mechanism by which the various species form. The first of these intermediates is assigned as an alkyl-Ni(III) species because it exhibits an absorption spectrum similar to that of the organonickel intermediates formed when MCR_red1 reacts with various alkyl halides including BPS and methyl iodide (*14, 17*). When reacted with thiolates (including HSCoM) (*12, 16, 28*), these

Table 1: Kinetic Parameters for the Three-Step Reaction Involving MCR_{red1} Radical Formation

	A → (k_1) B			B → (k_2) C	C → (k_3) D
	k_1 (s^{-1})	K_{m1} (mM)	k_1/K_{m1} (M^{-1} s^{-1})	k_2 (s^{-1})	k_3 (s^{-1})
CoB$_6$SH (+5 mM BES)	75 ± 6	1.7 ± 0.3	45000 ± 9000	2.6 ± 0.3	1.0 ± 0.1
BES (+1 mM CoB$_6$SH)	38 ± 1	0.7 ± 0.1	51500 ± 9900	2.8 ± 0.5	1.1 ± 0.1
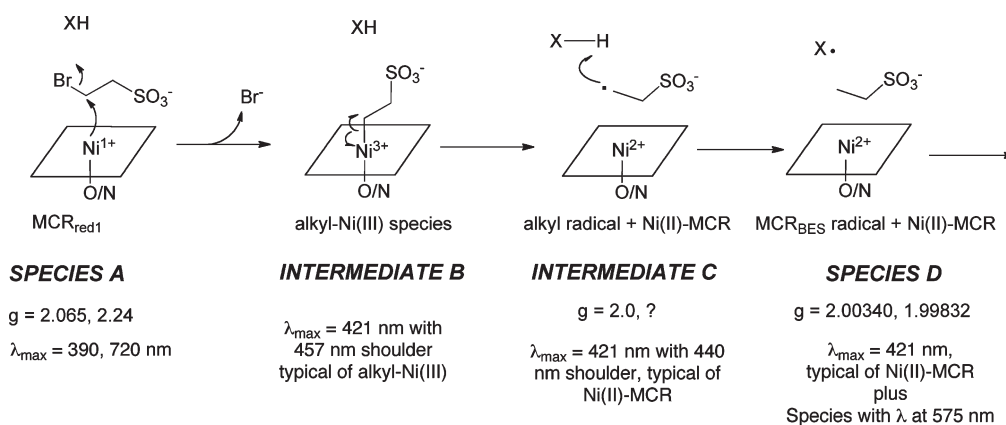
FIGURE 10: Proposed mechanism for MCR_{BES} radical formation. "X" is the species with the doublet radical EPR spectrum and the long wavelength absorption.

alkyl-Ni(III) species convert to the active MCR_{red1} state along with the corresponding alkane when protonolyzed or reduced with Ti(III) citrate (*14, 17*), supporting the catalytic intermediacy of the alkyl-Ni species in methane synthesis. Prior studies indicated that reactive haloalkyl compounds that are the size of HSCoM generate radicals, while those that are the size of methyl-SCoM (and larger) yield organometallic species. However, as shown here, the reaction with BES also generates an organometallic intermediate that rapidly converts to the characteristic MCR_{BES} radical. Therefore, the reaction of MCR with all haloalkanes may generate an initial organometallic species that converts to other intermediates at varying rates that determine whether or not these species accumulate to detectable levels. This organonickel species (B) quickly converts to a relatively stable radical labeled as X· in Figure 8 (species D, MCR_{BES}) through intermediate C, which was identified by global kinetic analysis. We propose that MCR_{BES} is formed by homolytic cleavage of the alkyl–Ni(III) bond to generate an unstable alkyl radical that would abstract a hydrogen atom from the precursor of X· (i.e., X–H).

Free radicals have been identified as intermediates in a number of enzymatic reactions (*55*). These radicals include amino acid-based radicals, such as the tyrosyl radical in class I ribonucleotide reductases (*52*) and in other enzymes (*49, 51, 53*), a cysteine-based thiyl radical in all three classes of ribonucleotide reductase (*55*), and a glycyl radical in pyruvate formate lyase (*56*). Furthermore, catalytic radicals are formed by various cofactors, e.g., the adenosyl radical (generated from S-adenosyl-L-methionine or adenosylcobalamin), a hydroxyethyl thiamine pyrophosphate radical in pyruvate ferredoxin oxidoreductase, and a porphyrin π-cation radical in chloroperoxidase (*55, 57, 58*).

Radicals have been proposed as key intermediates in the MCR-catalyzed synthesis of methane (*6, 22, 23*); however, so far such radicals have not been identified spectroscopically when MCR is reacted with its natural substrates. On the other hand, a radical EPR doublet signal (the MCR_{BES} radical) is generated when MCR_{red1} is reacted with BES in the presence of

CoB$_6$SH/CoBSH (*18*). We show here that MCR_{BES} is transiently formed and accumulates to a maximum of ~20% of the initial amount of MCR_{red1}.

Based on the crystal structure of MCR (*3*), it appears that several amino acids (Tyr and thioglycine), the corphin ring itself, and the sulfur group of its substrates, CoB$_6$SH/CoBSH or HSCoM, are reasonable candidates for XH, the precursor of the MCR_{BES} radical. Although the simplest explanation for the 575 nm absorption peak and the MCR_{BES} radical to accumulate over the same time frame is that they belong to the same species, another possibility is that the EPR and UV–visible spectra belong to different, but kinetically coupled, species. This is because transient kinetic experiments assign intermediates based on the dynamics of spectral evolution. For example, homolytic cleavage of alkyl-Ni(III) would generate the alkyl radical and a Ni(II) species, which would be assigned as a single intermediate by the global kinetic fitting protocol, because they form and decay at the same rate. According to this scenario, the UV–visible spectrum would be dominated by the Ni(II) component, and the EPR spectrum would reveal the radical. As described above, because two Tyr residues are situated just above the upper axial Ni ligand (the ethyl sulfonyl group in this case), we used EPR and ENDOR spectroscopy to test the possibility that the MCR_{BES} radical comes from Tyr.

Our EPR and ENDOR spectroscopic studies of the MCR_{BES} radical generated from [$^2H_6$]Tyr-labeled MCR rule out the possibility that the MCR_{BES} radical derives from tyrosine. First, the g-values of the MCR_{BES} radical ($g_\perp = 2.0034$ and $g_\parallel = 1.9983$) are not consistent with those typically observed for a Tyr radical which exhibits rhombic spectra with g_1 is in the range of 2.009–2.006, g_2 at 2.004–2.005, and g_3 at 2.002–2.003. The g-values of the MCR_{BES} radical are most consistent with a species with significant electron spin density localization on carbon, hydrogen, and/or nitrogen rather than oxygen and sulfur, since the latter would be expected to result in g-values > 2.005 (for sulfur-based radicals, see refs (*59–61*)). Furthermore, as described in the

Results section, because all tyrosyl radical spectra exhibit significant broadening or splitting from the hyperfine interactions of three or four nonexchangeable protons, the substitution of natural abundance Tyr by [^{2}H]Tyr would be expected to markedly alter the spectrum of any tyrosyl radical species. The lack of any observable difference in the EPR spectra of the MCR$_{BES}$ radical generated from enzyme containing [^{2}H]- versus [^{1}H]Tyr demonstrates conclusively that MCR$_{BES}$ is not a Tyr radical.

The visible spectrum, with a broad peak around 575 nm, is also inconsistent with a typical Tyr radical. For example, the primary absorption bands characteristic for a phenoxyl radical include a sharp intense band at ~410 nm ($\varepsilon > 1800$ M^{-1} cm^{-1}), another intense but broader band at ~390 nm ($\varepsilon > 900$ M^{-1} cm^{-1}), and a broad weak band at ~600 nm ($\varepsilon < 500$ M^{-1} cm^{-1}) (*62, 63*). Although the absorption spectrum is not consistent with a Tyr radical, it would not be inconsistent with that of a radical formed on the corphin ring of F$_{430}$. A porphyrin π-radical, which is coupled with an oxoiron(IV) heme species, has been reported in many hemoproteins (*57*) and has a characteristic absorbance in the range of 650−700 nm (*64*). Because the corphin ring contains only five double bonds, four of which are in conjugation, the absorption maxima of a corphin-based radical could shift to higher energies. However, as mentioned below, the EPR spectra are inconsistent with assigning the radical to the tetrapyrrole ring of F$_{430}$. Alternatively, as mentioned above, one can consider the possibility that the EPR and UV−visible spectra belong to different, but kinetically coupled, species.

Glycyl, tryptophanyl, ketyl, allyl, and other C/N based radicals as well as the corphin-based radical may have *g*-values in the range observed here, but these species have hyperfine couplings that either are not fully characterized or are inconsistent with those measured here. For example, although it is an otherwise attractive possibility given the long wavelength absorption (see below), it appears highly unlikely that the MCR$_{BES}$ radical derives from the corphin ring of F$_{430}$ because the Ni(II) center in MCR and in the free cofactor has an $S = 1$ configuration with a significant zero field splitting (*65*). Thus, such a radical would likely magnetically interact with the tetrapyrrole in a way that would lead to a significantly different EPR spectrum than that observed. Rather than being a narrow EPR signal at $g \approx 2.00$, a coupled radical would have substantial *g* anisotropy. It appears that the observed EPR spectrum could only arise from a tetrapyrrole-centered radical if the Ni(II) center were in the $S = 0$ configuration, which has no precedence in MCR forms. Thus, although a Tyr radical can be ruled out, further experiments, including isotopic substitutions, will be required to make a positive assignment for the MCR$_{BES}$ radical.

Even though MCR$_{BES}$ (X· in Figure 10) does not contain a tyrosyl radical, our results suggest that a tyrosyl residue may still play a role in formation of the MCR$_{BES}$ radical. Acetylation of tyrosyl residues greatly inhibits the reaction of MCR$_{red1}$ with BES, suggesting that a tyrosyl residue may be involved in formation of the MCR$_{BES}$ radical. The acetyl group may simply sterically hinder the reaction of Ni(I) with BES, and MCR$_{BES}$ may be formed by a pathway independent of the involvement of Tyr. However, another hypothesis that is consistent with our Tyr-modification results is that the stable doublet MCR$_{BES}$ radical with the long wavelength absorbance is generated by hydrogen atom abstraction from a transient Tyr radical. According to this scenario, the ethanesulfonyl radical (intermediate C) could abstract a hydrogen atom from one of the two nearby Tyr residues to form a tyrosyl radical that could rapidly abstract a

hydrogen atom from the corphin ring or one of the other species described above (CoBSH/CoB$_6$SH, thiogycine, HSCoM) to generate the MCR$_{BES}$ radical (species D). In this scenario, the Tyr radical would form and decay too rapidly to accumulate to detectable levels. The intermediacy of the Tyr radical is, of course, speculative since, thus far, the only radical we have observed is the relatively stable MCR$_{BES}$ radical with the doublet EPR spectrum.

The detection of both organonickel and radical species suggests a new mechanism for methane synthesis that combines the key features of mechanisms I (a methylnickel intermediate) and II (a methyl radical intermediate). Both mechanisms also predict that a thiyl radical from CoBSH is generated as an intermediate, but the EPR parameters of the MCR$_{BES}$ radical do not support a thiyl radical assignment for the doublet EPR signal. Because of the inhibitory effects of Tyr acetylation, we speculate that the stable radical is formed by abstraction of a H-atom from an initially formed Tyr radical. The final proposed steps in both mechanisms I and II involve a disulfide anion radical (CoBS-SCoM) that reduces the Ni(II) species (above) back to active MCR$_{red1}$. Our studies also provide evidence against a potential F$_{430}$-based radical, which was invoked in mechanism III.

Because no intermediates have been observed in various rapid kinetic studies of the reaction of MCR$_{red1}$ with the native substrates, it is important to identify the MCR$_{BES}$ radical by performing further isotope labeling studies. Recent experiments of the reaction of MCR$_{red1}$ with methyl-SCoM and CoB$_6$SH reveal a doublet radical, but with different UV−visible spectra than those of MCR$_{BES}$ (Dey and Ragsdale, unpublished). Thus, experiments similar to those described here may reveal the identity of an intermediate in the reaction with methyl-SCoM and CoBSH.

NOTE ADDED AFTER ASAP PUBLICATION

After this paper was published ASAP July 19, 2010, coauthor Ryan C. Kunz was added to the author list. The revised version was published July 22, 2010.

SUPPORTING INFORMATION AVAILABLE

Kinetics of MCR$_{BES}$ radical decay with BES and CoBSH as substrates (Figure S1), 35 GHz EPR spectra at 2 K of MCR$_{red1}$ in the presence 1 mM CoB$_6$SH after addition of BES (Figure S2), and broad scan swept CW 35 GHz ^{1}H ENDOR spectra of MCR$_{red1}$ recorded at 2 K at a field position on the MCR signal ($g = 2.177$, upper trace) and on the radical signal ($g = 2.002$, lower trace) (Figure S3). This material is available free of charge via the Internet at http://pubs.acs.org.

REFERENCES

1. DiMarco, A. A., Bobik, T. A., and Wolfe, R. S. (1990) Unusual coenzymes of methanogenesis. *Annu. Rev. Biochem. 59*, 355–394.
2. Thauer, R. K. (1998) Biochemistry of methanogenesis: a tribute to Marjory Stephenson. 1998 Marjory Stephenson Prize Lecture. *Microbiology 144* (Part 9), 2377–2406.
3. Ermler, U., Grabarse, W., Shima, S., Goubeaud, M., and Thauer, R. K. (1997) Crystal structure of methyl-coenzyme M reductase: the key enzyme of biological methane formation. *Science 278*, 1457–1462.
4. Mahlert, F., Bauer, C., Jaun, B., Thauer, R. K., and Duin, E. C. (2002) The nickel enzyme methyl-coenzyme M reductase from methanogenic archaea: in vitro induction of the nickel-based MCR-ox EPR signals from MCR-red2. *J. Biol. Inorg. Chem. 7*, 500–513.
5. Grabarse, W., Mahlert, F., Shima, S., Thauer, R. K., and Ermler, U. (2000) Comparison of three methyl-coenzyme M reductases from

phylogenetically distant organisms: unusual amino acid modification, conservation and adaptation. *J. Mol. Biol.* 303, 329–344.

6. Grabarse, W., Mahlert, F., Duin, E. C., Goubeaud, M., Shima, S., Thauer, R. K., Lamzin, V., and Ermler, U. (2001) On the mechanism of biological methane formation: structural evidence for conformational changes in methyl-coenzyme M reductase upon substrate binding. *J. Mol. Biol.* 309, 315–330.

7. Goubeaud, M., Schreiner, G., and Thauer, R. K. (1997) Purified methyl-coenzyme-M reductase is activated when the enzyme-bound coenzyme F$_{430}$ is reduced to the nickel(I) oxidation state by titanium(III) citrate. *Eur. J. Biochem.* 243, 110–114.

8. Albracht, S. P. J., Ankel-Fuchs, D., Böcher, R., Ellermann, J., Moll, J., van der Zwann, J. W., and Thauer, R. K. (1988) Five new EPR signals assigned to nickel in methyl-coenzyme M reductase from *Methanobacterium thermoautotrophicum*, strain Marburg. *Biochim. Biophys. Acta* 955, 86–102.

9. Rospert, S., Böcher, R., Albracht, S. P. J., and Thauer, R. K. (1991) Methyl-coenzyme M reductase preparations with high specific activity from H$_2$-preincubated cells of *Methanobacterium thermoautotrophicum*. *FEBS Lett.* 291, 371–375.

10. Goenrich, M., Duin, E. C., Mahlert, F., and Thauer, R. K. (2005) Temperature dependence of methyl-coenzyme M reductase activity and of the formation of the methyl-coenzyme M reductase red2 state induced by coenzyme B. *J. Biol. Inorg. Chem.* 10, 333–342.

11. Ellermann, J., Rospert, S., Thauer, R. K., Bokranz, M., Klein, A., Voges, M., and Berkessel, A. (1989) Methyl-coenzyme-M reductase from *Methanobacterium thermoautotrophicum* (strain Marburg). Purity, activity and novel inhibitors. *Eur. J. Biochem.* 184, 63–68.

12. Rospert, S., Voges, M., Berkessel, A., Albracht, S. P., and Thauer, R. K. (1992) Substrate-analogue-induced changes in the nickel-EPR spectrum of active methyl-coenzyme-M reductase from *Methanobacterium thermoautotrophicum*. *Eur. J. Biochem.* 210, 101–107.

13. Hinderberger, D., Piskorski, R. P., Goenrich, M., Thauer, R. K., Schweiger, A., Harmer, J., and Jaun, B. (2006) A nickel-alkyl bond in an inactivated state of the enzyme catalyzing methane formation. *Angew. Chem., Int. Ed. Engl.* 45, 3602–3607.

14. Dey, M., Telser, J., Kunz, R. C., Lees, N. S., Ragsdale, S. W., and Hoffman, B. M. (2007) Biochemical and spectroscopic studies of the electronic structure and reactivity of a methyl-Ni species formed on methyl-coenzyme M reductase. *J. Am. Chem. Soc.* 129, 11030–11032.

15. Yang, N., Reiher, M., Wang, M., Harmer, J., and Duin, E. C. (2007) Formation of a nickel-methyl species in methyl-coenzyme M reductase, an enzyme catalyzing methane formation. *J. Am. Chem. Soc.* 129, 11028–11029.

16. Dey, M., Kunz, R. C., Lyons, D. M., and Ragsdale, S. W. (2007) Characterization of alkyl-nickel adducts generated by reaction of methyl-coenzyme m reductase with brominated acids. *Biochemistry* 46, 11969–11978.

17. Kunz, R. C., Horng, Y. C., and Ragsdale, S. W. (2006) Spectroscopic and kinetic studies of the reaction of bromopropanesulfonate with methyl-coenzyme M reductase. *J. Biol. Chem.* 281, 34663–34676.

18. Goenrich, M., Mahlert, F., Duin, E. C., Bauer, C., Jaun, B., and Thauer, R. K. (2004) Probing the reactivity of Ni in the active site of methyl-coenzyme M reductase with substrate analogues. *J. Biol. Inorg. Chem.* 9, 691–705.

19. Gunsalus, R. P., Romesser, J. A., and Wolfe, R. S. (1978) Preparation of coenzyme M analogues and their activity in the methylcoenzyme M reductase system of *Methanobacterium thermoautotrophicum*. *Biochemistry* 17, 2374–2377.

20. Ellermann, J., Hedderich, R., Böcher, R., and Thauer, R. K. (1988) The final step in methane formation. Investigations with highly purified methyl-CoM reductase (component C) from *Methanobacterium thermoautotrophicum* (strain Marburg). *Eur. J. Biochem.* 172, 669–677.

21. Immig, I., Demeyer, D., Fiedler, D., Van Nevel, C., and Mbanzamihigo, L. (1996) Attempts to induce reductive acetogenesis into a sheep rumen. *Arch. Tierernahr.* 49, 363–370.

22. Signor, L., Knuppe, C., Hug, R., Schweizer, B., Pfaltz, A., and Jaun, B. (2000) Methane formation by reaction of a methyl thioether with a photo-excited nickel thiolate—a process mimicking methanogenesis in archaea. *Chemistry* 6, 3508–3516.

23. Pelmenschikov, V., Blomberg, M. R., Siegbahn, P. E., and Crabtree, R. H. (2002) A mechanism from quantum chemical studies for methane formation in methanogenesis. *J. Am. Chem. Soc.* 124, 4039–4049.

24. Duin, E. C., and McKee, M. L. (2008) A new mechanism for methane production from methyl-coenzyme M reductase as derived from density functional calculations. *J. Phys. Chem. B* 112, 2466–2482.

25. Lin, S.-K., and Jaun, B. (1991) Coenzyme F430 from methanogenic bacteria: detection of a paramagnetic methylnickel(II) derivative of

the pentamethyl easter by ^{2}H-NMR spectroscopy. *Helv. Chim. Acta* 74, 1725–1738.

26. Lin, S.-K., and Jaun, B. (1992) Coenzyme F430 from methanogenic bacteria: mechanistic studies on the reductive cleavage of sulonium ions catalyzed by F430 pentamethyl ester. *Helv. Chim. Acta* 75, 1478–1490.

27. Lahiri, G. K., Schussel, L. J., and Stolzenberg, A. M. (1992) F430 model chemistry. Mechanistic investigation of the reduction, coupling, and dehydrohalogenation of alkyl halides by the nickel(I) octaethylisobacteriochlorin anion. *Inorg. Chem.* 31, 4991–5000.

28. Kunz, R. C., Dey, M., and Ragsdale, S. W. (2008) Characterization of the thioether product formed from the thiolytic cleavage of the alkyl-nickel bond in methyl-coenzyme M reductase. *Biochemistry* 47, 2661–2667.

29. Pelmenschikov, V., and Siegbahn, P. E. (2003) Catalysis by methyl-coenzyme M reductase: a theoretical study for heterodisulfide product formation. *J. Biol. Inorg. Chem.* 8, 653–662.

30. Chen, S. L., Pelmenschikov, V., Blomberg, M. R., and Siegbahn, P. E. (2009) Is there a Ni-methyl intermediate in the mechanism of methyl-coenzyme M reductase? *J. Am. Chem. Soc.* 131, 9912–9913.

31. Bobik, T. A., and Wolfe, R. S. (1988) Physiological importance of the heterodisulfide of coenzyme M and 7-mercaptoheptanoylthreonine phosphate in the reduction of carbon dioxide to methane in Methanobacterium. *Proc. Natl. Acad. Sci. U.S.A.* 85, 60–63.

32. Noll, K. M., Donnelly, M. I., and Wolfe, R. S. (1987) Synthesis of 7-mercaptoheptanoylthreonine phosphate and its activity in the methyl-coenzyme M methylreductase system. *J. Biol. Chem.* 262, 513–515.

33. Porat, I., Sieprawska-Lupa, M., Teng, Q., Bohanon, F. J., White, R. H., and Whitman, W. B. (2006) Biochemical and genetic characterization of an early step in a novel pathway for the biosynthesis of aromatic amino acids and p-aminobenzoic acid in the archaeon *Methanococcus maripaludis*. *Mol. Microbiol.* 62, 1117–1131.

34. Telser, J. (2007) Electron-nuclear double resonance (ENDOR) spectroscopy, in Applications of Physical Methods to Inorganic and Bioinorganic Chemistry (Scott, R. A., and Lukehart, C. M., Eds.) pp 99−124, John Wiley & Sons, Chichester, U.K.

35. Mailer, C., and Taylor, C. P. S. (1973) Rapid adiabatic passage EPR of ferricytochrome *c*. Signal enhancement and determination of the spin-lattice relaxation time. *Biochim. Biophys. Acta* 322, 195–203.

36. Werst, M. M., Davoust, C. E., and Hoffman, B. M. (1991) Ligand spin densities in blue copper proteins by Q-band ^{1}H and ^{14}N ENDOR spectroscopy. *J. Am. Chem. Soc.* 113, 1533–1538.

37. Davoust, C. E., Doan, P. E., and Hoffman, B. M. (1996) Q-band pulsed electron spin-echo spectrometer and its application to ENDOR and ESEEM. *J. Magn. Reson.* 119, 38–44.

38. Lee, H.-I., Igarashi, R. Y., Laryukhin, M., Doan, P. E., Dos Santos, P. C., Dean, D. R., Seefeldt, L. C., and Hoffman, B. M. (2004) An organometallic intermediate during alkyne reduction by nitrogenase. *J. Am. Chem. Soc.* 126, 9563–9569.

39. Doan, P. E., Gurbiel, R. J., and Hoffman, B. M. (2007) The ups and downs of Feher-style ENDOR. *Appl. Magn. Reson.* 31, 647–661.

40. Schweiger, A., and Jeschke, G. (2001) Principles of Pulse Electron Paramagnetic Resonance, Oxford University Press, Oxford, U.K.

41. Krymov, V., and Gerfen, G. J. (2003) Analysis of the tuning and operation of reflection resonator EPR spectrometers. *J. Magn. Reson.* 162, 466–478.

42. Ranguelova, K., Girotto, S., Gerfen, G. J., Yu, S., Suarez, J., Metlitsky, L., and Magliozzo, R. S. (2007) Radical sites in *Mycobacterium tuberculosis* KatG identified using electron paramagnetic resonance spectroscopy, the three-dimensional crystal structure, and electron transfer couplings. *J. Biol. Chem.* 282, 6255–6264.

43. Harmer, J., Finazzo, C., Piskorski, R., Bauer, C., Jaun, B., Duin, E. C., Goenrich, M., Thauer, R. K., Doorslaer, S. V., and Schweiger, A. (2005) Spin density and coenzyme M coordination geometry of the ox1 form of methyl-coenzyme M reductase: a pulse EPR study. *J. Am. Chem. Soc.* 127, 17744–17755.

44. Craft, J. L., Horng, Y.-C., Ragsdale, S. W., and Brunold, T. C. (2004) Nickel oxidation states of F$_{430}$ cofactor in methyl-coenzyme M reductase. *J. Am. Chem. Soc.* 126, 4068–4069.

45. Finazzo, C., Harmer, J., Jaun, B., Duin, E. C., Mahlert, F., Thauer, R. K., Doorslaer, S. V., and Schweiger, A. (2003) Characterization of the MCR$_{red2}$ form of methyl-coenzyme M reductase: a pulse EPR and ENDOR study. *J. Biol. Inorg. Chem.* 8, 586–593.

46. Hyde, J. S., and Froncisz, W. (1982) The role of microwave frequency in EPR spectroscopy of copper complexes. *Annu. Rev. Biophys. Bioeng.* 11, 391–417.

47. Harmer, J., Finazzo, C., Piskorski, R., Ebner, S., Duin, E. C., Goenrich, M., Thauer, R. K., Reiher, M., Schweiger, A., Hinderberger,

D., and Jaun, B. (2008) A nickel hydride complex in the active site of methyl-coenzyme M reductase: implications for the catalytic cycle. *J. Am. Chem. Soc. 130*, 10907–10920.

48. Dorlet, P., Valentin, M. D., Babcock, G. T., and McCracken, J. L. (1998) Interaction of $Y_Z\cdot$ with its environment in acetate-treated photosystem ii membranes and reaction center cores. *J. Phys. Chem. B 102*, 8239–8247.

49. Hoganson, C. W., and Babcock, G. T. (1992) Protein-tyrosyl radical interactions in photosystem II studied by electron spin resonance and electron nuclear double resonance spectroscopy: comparison with ribonucleotide reductase and in vitro tyrosine. *Biochemistry 31*, 11874–11880.

50. Shi, W., Hoganson, C. W., Espe, M., Bender, C. J., Babcock, G. T., Palmer, G., Kulmacz, R. J., and Tsai, A.-l. (2000) Electron paramagnetic resonance and electron nuclear double resonance spectroscopic identification and characterization of the tyrosyl radicals in prostaglandin H synthase 1. *Biochemistry 39*, 4112–4121.

51. Dorlet, P., Seibold, S. A., Babcock, G. T., Gerfen, G. J., Smith, W. L., Tsai, A.-l., and Un, S. (2002) High-field EPR study of tyrosyl radicals in prostaglandin H_2 synthase-1. *Biochemistry 41*, 6107–6114.

52. Hoganson, C. W., Sahlin, M., Sjöberg, B.-M., and Babcock, G. T. (1996) Electron magnetic resonance of the tyrosyl radical in ribonucleotide reductase from *Escherichia coli. J. Am. Chem. Soc. 118*, 4672–4679.

53. Whittaker, J. W. (2003) Free radical catalysis by galactose oxidase. *Chem. Rev. 103*, 2347–2364.

54. Gerfen, G. J., Bellew, B. F., Griffin, R. G., Singel, D. J., Ekberg, C. A., and Whittaker, J. W. (1996) High-frequency electron paramagnetic resonance spectroscopy of the apogalactose oxidase radical. *J. Phys. Chem. 100*, 16739–16748.

55. Stubbe, J., and van Der Donk, W. A. (1998) Protein radicals in enzyme catalysis. *Chem. Rev. 98*, 705–762.

56. Wagner, A. F., Frey, M., Neugebauer, F. A., Schafer, W., and Knappe, J. (1992) The free radical in pyruvate formate-lyase is located on glycine-734. *Proc. Natl. Acad. Sci. U.S.A. 89*, 996–1000.

57. Sono, M., Roach, M. P., Coulter, E. D., and Dawson, J. H. (1996) Heme-containing oxygenases. *Chem. Rev. 96*, 2841–2888.

58. Frey, P. A., Hegeman, A. D., and Reed, G. H. (2006) Free radical mechanisms in enzymology. *Chem. Rev. 106*, 3302–3316.

59. Symons, M. C. R. (1974) On the electron spin resonance detection of RS radicals in irradiated solids: radicals of type $RSSR^-$, $RS\text{-}SR_2$, and $R_2SSR_2^+$. *J. Chem. Soc., Perkin Trans. 2*, 1618–1620.

60. Gastel, M. v., Lubitz, W., Lassmann, G., and Neese, F. (2004) Electronic structure of the cysteine thiyl radical: a DFT and correlated ab initio study. *J. Am. Chem. Soc. 126*, 2237–2246.

61. Lassmann, G., Kolberg, M., Bleifuss, G., Gräslund, A., Sjöberg, B.-M., and Lubitz, W. (2003) Protein thiyl radicals in disordered systems: a comparative EPR study at low temperature. *Phys. Chem. Chem. Phys. 5*, 2442–2453.

62. Larsson, A., and Sjoberg, B. M. (1986) Identification of the stable free radical tyrosine residue in ribonucleotide reductase. *EMBO J. 5*, 2037–2040.

63. Petersson, L., Graslund, A., Ehrenberg, A., Sjoberg, B. M., and Reichard, P. (1980) The iron center in ribonucleotide reductase from *Escherichia coli. J. Biol. Chem. 255*, 6706–6712.

64. Svistunenko, D. A. (2005) Reaction of haem containing proteins and enzymes with hydroperoxides: the radical view. *Biochim. Biophys. Acta 1707*, 127–155.

65. Cheesman, M. R., Ankel-Fuchs, D., Thauer, R. K., and Thomson, A. J. (1989) The magnetic properties of the nickel cofactor F430 in the enzyme methyl-coenzyme M reductase of *Methanobacterium thermoautotrophicum. Biochem. J. 260*, 613–616.